

# A Method for Stereological Determination of the Structure Function From Histological Sections of Isotropic Scattering Media

Aiguo Han , *Member, IEEE*

**Abstract**—The frequency-dependent ultrasonic backscatter coefficient (BSC) from tissues, a fundamental parameter estimated by quantitative ultrasound (QUS) techniques, contains microstructure information useful for tissue characterization. To extract the microstructure information from the BSC, the tissue under investigation is often modeled as a collection of discrete scatterers embedded in a homogeneous background. From a discrete scatterer point of view, the BSC is dependent on not only the properties of individual scatterers relative to the background but also the scatterer spatial arrangement [described by the structure function (SF)]. Recently, the 2-D SF was computed from histological tissue sections, and was shown to be related to the volumetric SF extracted from QUS measurements. In this paper, a stereological method is proposed to extract the volumetric (3-D) SF from 2-D histological tissue sections. Simulations and experimental cell pellet biophantom studies were conducted to evaluate the proposed method. Simulation results verified the proposed method. Experimental results showed that the volumetric SF extracted using the proposed method had a significantly better agreement with the QUS-extracted SF than did the 2-D SF extracted in the previous study. The proposed stereological approach provides a useful tool for predicting the SF from histology.

**Index Terms**—Acoustic scattering, backscatter coefficient (BSC), stereology, structure function (SF).

## I. INTRODUCTION

QUANTITATIVE ultrasound (QUS) techniques have been investigated for tissue characterization in many organs such as the eye [1], [2], prostate [3], kidney [4], heart [5], [6], blood [7], [8], breast [9]–[12], liver [13], and lymph nodes [14], and for various applications such as apoptosis detection [15], [16], breast cancer characterization [17] and treatment monitoring [18], liver steatosis detection [19]–[21], and preterm birth prediction [22].

One of the QUS approaches utilizes signal processing strategies to estimate the frequency-dependent ultrasonic backscatter coefficient (BSC) from the radio frequency echo data. The system- and operator-independent BSC contains tissue microstructure information that is unavailable from the

conventional gray-scale B-mode ultrasound images. A model-based approach can be used to extract such information from the BSC. Understanding the ultrasonic scattering mechanism(s) in biological tissues is thus essential for accurately modeling the BSC and improving the sensitivity and specificity of QUS techniques.

The tissue under investigation is often modeled as the collection of discrete scatterers embedded in a homogeneous background. Under the discrete scatterer assumption, the BSC is dependent on the properties of individual scatterers relative to the background, modeled by the form factor [23]. The BSC is also dependent on the spatial arrangement of the scatterers because of phase interference, described by the structure function (SF) as a factor in the BSC expression [24], [25]. The form factor has been extensively studied. Various form factor models (e.g., fluid sphere [23], Gaussian [23], spherical shell [23], and concentric spheres [10], [26], [27]) have been developed and applied to biological tissues. These models yield tissue microstructure parameters such as the effective scatterer diameter and effective acoustic concentration that are sensitive to various disease conditions. In contrast, the SF has not been sufficiently studied in the context of ultrasonic scattering from tissues. The SF is related to the squared modulus of the Fourier transform of scatterer positions. It approaches unity if the scatterer positions are independent with each other, and shows a frequency-dependent interference pattern when the scatterer positions are correlated, for instance, when the scatterer concentration is high, or when scatterers are arranged in special patterns. Originally developed in statistical mechanics, the SF was first introduced in the field of acoustic scattering by Twersky [24], [28], and first implemented for describing biological scatterers by Fontaine *et al.* [25]. Subsequent studies have shown that the SF has a strong effect on scattering in aggregated red blood cells [29]–[32], cell apoptosis [33], [34], concentrated tissue-mimicking phantoms [35], concentrated cell pellet biophantoms [27], [36]–[38], and various solid tumors [39]–[41].

Recently, the 2-D SF was calculated from histological sections, and was shown to be related to the volumetric SF extracted from QUS measurements [41]. Estimating the SF from histology was pursued for several reasons. First, estimating the SF from histology has theoretical values of elucidating the ultrasonic scattering mechanism(s) in biological media, because the histology-derived and QUS-derived SFs can be

Manuscript received January 30, 2018; accepted March 18, 2018. Date of publication March 21, 2018; date of current version June 1, 2018. This work was supported by the National Institutes of Health under Grant R37EB002641 and Grant R01DK106419.

The author is with the Biocoustics Research Laboratory, Department of Electrical and Computer Engineering, University of Illinois, Urbana, IL 61801 USA (e-mail: han51@illinois.edu).

Digital Object Identifier 10.1109/TUFFC.2018.2818071

directly compared. Second, it provides a basis to develop analytical SF models for various tissue types. Third, it provides a research tool to predict whether QUS-derived SF is sensitive to a disease condition by analyzing the clinically available hematoxylin and eosin (H&E)-stained histology.

While [41] demonstrated the correlation between histology-derived and QUS-derived SFs, the agreement between the two was not perfect. Indeed, the histology-derived SF was 2-D, whereas the QUS-derived SF was volumetric (3-D). A critical question to be answered is whether it is possible to derive the volumetric SF from 2-D histological sections and (if possible) how the performance of the histology-derived volumetric SF compares with that of the simple 2-D SF.

To answer this question, a stereological method is proposed herein to extract the volumetric SF from 2-D histological tissue sections. The proposed method derives the 3-D SF from a 2-D cross section by utilizing the relationship between SF and pair correlation function and the stereological relationship between 2-D and 3-D pair correlation functions. The 3-D SF is derived from the 3-D pair correlation function that is derived from the 2-D pair correlation function calculated from a 2-D point distribution. Simulations and experimental cell pellet studies are also discussed to evaluate the proposed method.

The rest of this paper is organized as follows. The theoretical background is introduced in Section II. Section III describes the proposed method in detail. Section IV presents the simulation that verifies the proposed method. Section V applies the proposed method to cell pellet biophantom data and discusses the method. Section VI concludes this paper.

## II. THEORY

### A. Backscatter Coefficient

When a plane wave of unit amplitude is incident on a scattering volume  $V$  that contains  $N$  discrete scatterers, the far-field response behaves as a spherical wave [23]

$$p_s(\mathbf{r}) = \frac{e^{ikr}}{R} \sum_{j=1}^N \Phi_j(\mathbf{K}) e^{i\mathbf{K}\cdot\mathbf{r}_j} \quad (1)$$

where  $p_s(\mathbf{r})$  is the scattered acoustic pressure at position  $\mathbf{r}$ ,  $R = |\mathbf{r}|$ ,  $\mathbf{r}_j$  is the position of the  $j$ th scatterer, and  $k$  is the propagation constant ( $k = \omega/c$  where  $\omega$  is the angular frequency and  $c$  is the propagation speed). The factor  $\Phi_j(\mathbf{K})$  is the complex scattering amplitude of the  $j$ th scatterer, and  $\mathbf{K}$  is the scattering vector with the magnitude given by  $|\mathbf{K}| = 2k \sin(\theta/2)$ , where  $\theta$  is the scattering angle ( $\theta = \pi$  for backscattering).  $\Phi_j$  is dependent on the properties of individual scatterers relative to the background.

The differential cross section per unit volume  $\sigma_d$  (i.e., the power scattered into a unit solid angle observed far from the scattering volume divided by the product of the incident intensity and the scattering volume) may be expressed as

$$\sigma_d(\mathbf{K}) = \frac{R^2 I_s}{V I_0} = \frac{1}{V} \left| \sum_{j=1}^N \Phi_j(\mathbf{K}) e^{i\mathbf{K}\cdot\mathbf{r}_j} \right|^2 \quad (2)$$

where  $I_s$  and  $I_0$  denote the scattering intensity and incident intensity, respectively.

BSC is defined as the differential cross section per unit volume in the backscattering direction ( $|\mathbf{K}| = 2k$ ).

### B. Structure Function

If the scatterers are spatially uncorrelated, the phase terms  $e^{i\mathbf{K}\cdot\mathbf{r}_j}$  in (2) are also uncorrelated. The differential cross section per unit volume for this case is expressed as

$$\sigma_{d,\text{incoherent}}(\mathbf{K}) = \frac{1}{V} \sum_{j=1}^N |\Phi_j(\mathbf{K})|^2. \quad (3)$$

If the scatterers are spatially correlated and the scattering amplitudes  $\Phi_j(\mathbf{K})$  are identical for all the scatterers, then (2) may be simplified as

$$\sigma_d(\mathbf{K}) = \bar{n} |\Phi_j(\mathbf{K})|^2 \frac{1}{N} \left( \sum_{j=1}^N e^{i\mathbf{K}\cdot\mathbf{r}_j} \right) \left( \sum_{j=1}^N e^{-i\mathbf{K}\cdot\mathbf{r}_j} \right) \quad (4)$$

where  $\bar{n} = N/V$  is the number density of the scatterers. Dividing (4) by (3) yields the SF

$$S(\mathbf{K}) = \frac{1}{N} \left( \sum_{j=1}^N e^{i\mathbf{K}\cdot\mathbf{r}_j} \right) \left( \sum_{j=1}^N e^{-i\mathbf{K}\cdot\mathbf{r}_j} \right) = \frac{1}{N} \left| \sum_{j=1}^N e^{-i\mathbf{K}\cdot\mathbf{r}_j} \right|^2. \quad (5)$$

An SF of unity corresponds to uncorrelated random scatterer positioning, and SF values above unity mean constructive interferences, whereas values below unity mean destructive interferences due to the scatterer positioning.

### C. Pair Correlation Function

In statistical mechanics, the pair correlation function  $g(r)$ , also called radial distribution function, describes the statistical distribution of a system of particles (or scatterers). Pair correlation function of a system of particles is a measure of the probability to find a particle in a shell of thickness  $dr$  at the distance  $r$  away from a given reference particle, relative to that for an ideal gas (where particle positions are assumed to be uncorrelated with each other).

Pair correlation function is introduced herein because it is related to the SF by [24]

$$S(\mathbf{K}) = 1 + \bar{n} \int [g(\mathbf{r}) - 1] e^{-i\mathbf{K}\cdot\mathbf{r}} d\mathbf{r}. \quad (6-a)$$

For 2-D and 3-D isotropic cases, (6-a) can be expressed as

$$S_A(2k) = 1 + 2\pi \bar{n}_A \int_0^\infty [g_A(r) - 1] r J_0(2kr) dr \quad (6-b)$$

and

$$S_V(2k) = 1 + 4\pi \bar{n}_V \int_0^\infty [g_V(r) - 1] r^2 \frac{\sin(2kr)}{2kr} dr \quad (6-c)$$

respectively, where the subscripts  $A$  and  $V$  represent 2-D (area) and 3-D (volume) quantities, respectively,  $\bar{n}_A$  is the 2-D number density (number of section disks per unit area),  $\bar{n}_V$  is the 3-D number density (number of particles per unit volume), and  $J_0$  is the zeroth-order Bessel function of the first kind.

#### D. Stereology

Quantitative stereology attempts to characterize 3-D features of the microstructure using 2-D cross sections of materials or tissues. The mathematical foundations of quantitative stereology can be found in [42].

For an isotropic distribution of nonoverlapping spheres, the relationship between the area (2-D) pair correlation function  $g_A(r)$  and the volumetric (3-D) pair correlation function  $g_V(r)$  can be expressed in the form of Hanisch's integral equation [43], [44]

$$g_A(r) = \int_0^\infty f_V(x, t) g_V(\sqrt{r^2 + x^2}) dx \quad \text{for } r \geq 0 \quad (7-a)$$

where

$$f_V(x, t) = \frac{2}{(d_V + t)^2} \times \int_0^\infty (1 - D_V([|x - u| - t]^+)) \times (1 - D_V([x + u - t]^+)) du \quad \text{for } x \geq 0 \quad (7-b)$$

where  $[x]^+ = \max\{x, 0\}$ ,  $d_V$  is the mean sphere diameter,  $D_V$  is the cumulative density distribution of the sphere diameter, and  $t$  is the section thickness.

For the special case of monodisperse spheres, (7) is simplified to

$$g_A(r) = \frac{2}{(d_V + t)^2} \int_0^{d_V + t} (d_V + t - x) g_V(\sqrt{r^2 + x^2}) dx \quad \text{for } r \geq 0. \quad (8)$$

### III. PROPOSED STEREOLOGICAL METHOD

#### A. Overview of the Proposed Method

Following the theories reviewed in Section II, a four-step stereological method is proposed to extract the volumetric SF from histological sections, under the assumption that the scatterers are nonoverlapping and spherical in shape, and the 3-D spatial distribution is isotropic.

*Step 1:* Process the histological image by applying shrinkage correction and fitting circles to the scatterers on the image.

*Step 2:* Calculate the 2-D pair correlation function using the fitted circle centers.

*Step 3:* Estimate the 3-D pair correlation function from the 2-D pair correlation function by numerically solving Hanisch's integral equation.

*Step 4:* Calculate the 3-D SF from the 3-D pair correlation function using (6-c).

The details are explained step by step in the remaining of Section III.

#### B. Histological Image Processing

A typical procedure to obtain histological images involves fixing the biological material (e.g., tissue) with some fixative (e.g., buffered formalin) for a certain period of time, embedding the fixed sample in paraffin, sectioning the paraffin-embedded sample, mounting the tissue sections on glass slides, and staining the tissue section (typically with H&E). The fixing step introduces tissue shrinkage. For instance, neutral-buffered formalin fixation has been shown to reduce the

linear dimension of the cells, nuclei, and whole tissue by approximately 10% compared to fresh samples [45], [46]. This shrinkage effect may be corrected by applying a shrinkage factor that is appropriate for the types of fixative and tissue under investigation.

In addition to shrinkage correction, a critical step in histological imaging processing is to fit circles to hypothetical scatterers on the histological image. The fitted circle centers are needed for 2-D pair correlation calculation in Step 2, and the fitted circle diameters will be used for sphere diameter estimation that is needed in Step 3.

The scatterer of interest is determined case by case. In cell pellet biophantoms (cells embedded in bovine plasma and thrombin clot [26]) and solid tumors, the scatterer of interest can be the cell nuclei or whole cells. If there is more than one candidate scatterer, then each candidate can be evaluated separately. In this case, the proposed method may also serve as a tool for identifying the scatterers from multiple candidates.

There are various circle fitting algorithms available in image processing, and the Hough transform is a practical method for finding circles. The Hough transform circle finding is implemented in the MATLAB library function "imfindcircles", which is used in this paper.

#### C. 2-D Pair Correlation Function Estimation

The 2-D pair correlation function  $g_A(r)$  is estimated using the algorithm described in [47] and briefly summarized as follows. The algorithm starts with choosing a distance step size  $dr$  that is small enough to avoid blurring any important structure in the pair correlation function curve while large enough to avoid counting too few scatterers in every step. For each distance  $r$  at which  $g_A(r)$  is to be calculated, each scatterer center is chosen in turn as a reference point. The number of centers that are at a distance between  $r$  and  $r + dr$  away from the reference center is counted, and averaged for all the reference centers. This number is then normalized by  $2\pi r dr$  (the area of the ring), and divided by the average number of centers per unit area. For reference centers near the image edge, the circle of some radius  $r$  may extend outside the image. This edge effect is correctly accounted for by determining how much angular extent of the circle lies within the image.

#### D. 3-D Pair Correlation Function Estimation

The 3-D pair correlation function is estimated from the 2-D pair correlation function by solving Hanisch's integral equation. A stereological estimation of the sphere size is needed before Hanisch's integral equation can be solved. The mean sphere diameter  $d_V$  is a parameter in (7) and (8), and the sphere diameter distribution  $D_V$  appears in (7).

If the planar section has zero thickness, a simple stereological estimator for the mean sphere diameter  $d_V$  is [44]

$$\hat{d}_V = \frac{N\pi}{2} \left/ \sum_{i=1}^N \frac{1}{d_i} \right. \quad (9)$$

where  $d_i$  is the diameter of the  $i$ th disk measured from a planar section,  $N$  is the total number of disks on the planar section.

If the section thickness is nonzero, the mean sphere diameter  $d_V$  is estimated as follows. The moments of the sphere diameter distribution are related to the moments of the disk diameter distribution by [48]

$$\bar{n}_V \tau_i = \bar{n}_A \sum_{k=0}^{\infty} \frac{p_{ik} \sigma_{i+k}}{t^{k+1}}, \quad i = 0, 1, \dots \quad (10)$$

where  $\tau_i$  is the  $i$ th order moment of the sphere diameter distribution (i.e.,  $\tau_0 = 1$ ,  $\tau_1 = d_V$ ),  $\sigma_{i+k}$  is the  $(i+k)$ th order moment of the disk diameter distribution measured from 2-D sections,  $t$  is the section thickness, and the coefficients  $p_{ik}$  are defined by

$$p_{i,0} = 1$$

$$p_{i,k} = (-1)^k \prod_{j=1}^k \left[ \frac{1}{2} \Gamma\left(\frac{i+j+1}{2}\right) \Gamma\left(\frac{1}{2}\right) \right. \\ \left. / \Gamma\left(\frac{i+j+2}{2}\right) \right], \quad k = 1, 2, \dots$$

where  $\Gamma$  is the gamma function. Applying the moment relationship (10) for  $i = 0$  and  $i = 1$  yields an estimator for the mean sphere diameter for the case of nonzero thickness

$$\hat{d}_V = \sum_{k=0}^{\infty} \frac{p_{1k} \sigma_{1+k}}{t^{k+1}} / \sum_{k=0}^{\infty} \frac{p_{0k} \sigma_k}{t^{k+1}}. \quad (11)$$

Equations (10) and (11) are used in the simulation study (Section IV) for  $t = 0$  and  $3 \mu\text{m}$ , respectively. Equation (11) is used in the biophantom study (Section V) for the histological sections with  $t = 3 \mu\text{m}$ .

There are no simple estimators available for the sphere diameter distribution function  $D_V$ , although model-based methods are available to estimate the sphere diameter distribution by assuming various distribution models [44], [48]. A monodisperse distribution is used in this paper for simplicity. Although the cell or nucleus diameter has a finite distribution, the distribution is considered narrow enough to be modeled as a monodisperse distribution for the purposes of solving Hanisch's integral equation, as verified by the simulation study discussed in Section IV.

Hanisch's integral equation is solved numerically. The numerical solution under the zero thickness condition was described in [49]. The numerical solution for a nonzero thickness is derived as follows. Making a change of variables  $z = (r^2 + x^2)^{1/2}$  to (7-a) and assuming that the function  $g_V(z)$  remains sufficiently constant over some small interval  $[z - \delta z/2, z + \delta z/2]$ , the integral equation (7-a) is changed to the matrix equation

$$g_A(r) = \frac{2}{(d_V + t)^2} \sum_{z \geq r} g_V(z) I(z, r) \quad (12)$$

where

$$I(z, r) = \int_{z_1}^{z_2} f_V(z, t) du$$

$$z_1 = \begin{cases} \sqrt{(z - \delta z/2)^2 - r^2}, & (z - \delta z/2)^2 > r^2 \\ 0, & \text{otherwise} \end{cases}$$

$$z_2 = \begin{cases} \sqrt{(z + \delta z/2)^2 - r^2}, & (z + \delta z/2)^2 > r^2 \\ 0, & \text{otherwise.} \end{cases} \quad (13)$$

The integral  $I(z, r)$  is dependent on the sphere diameter distribution. For the special case of identical sphere diameters, we have

$$I(z, r) = (\min\{z_2, z_{\max}\} - \min\{z_1, z_{\max}\}) \\ \times [d_V + t - 0.5(\min\{z_2, z_{\max}\} + \min\{z_1, z_{\max}\})] \quad (14)$$

and

$$z_{\max} = \sqrt{(d_V + t)^2 + r^2}. \quad (15)$$

The matrix equation (12) has desirable numerical properties. The matrix  $I(z, r)$  is upper triangular, and is also strongly diagonal for large values of  $r$ , which makes the numerical solution practical.

#### E. Volumetric Structure Function Estimation

The 3-D SF is calculated through (6-c) using the 3-D pair correlation function estimated in Step 3. The 3-D number density  $\bar{n}_V$  in (6-c) needs to be estimated prior to using (6-c). The 3-D number density  $\bar{n}_V$  is related to the 2-D number density  $\bar{n}_A$  by [44]

$$\bar{n}_V = \bar{n}_A / (d_V + t) \quad (16)$$

where the 2-D number density  $\bar{n}_A$  is estimated through circle fitting in Step 1 and  $d_V$  is estimated using (10) (zero thickness) or (11) (nonzero thickness).

## IV. SIMULATIONS

### A. Simulation Overview

Simulations were performed to evaluate the proposed method under various sphere diameters and diameter distribution widths, and with zero and nonzero section thicknesses. The simulations also serve the purpose of assessing the monodisperse distribution approximation used to solve Hanisch's equation for spheres having a distribution similar to that of cells and nuclei. Also, the robustness of the model is studied through simulation.

The overall idea of the simulation study was to computationally generate a 3-D distribution of nonoverlapping spheres, calculate the volumetric SF from the 3-D distribution as the ground truth, estimate 2-D SF and 3-D SF from 2-D slices of the 3-D volume, and compare the estimated 2-D and 3-D SFs with ground truth.

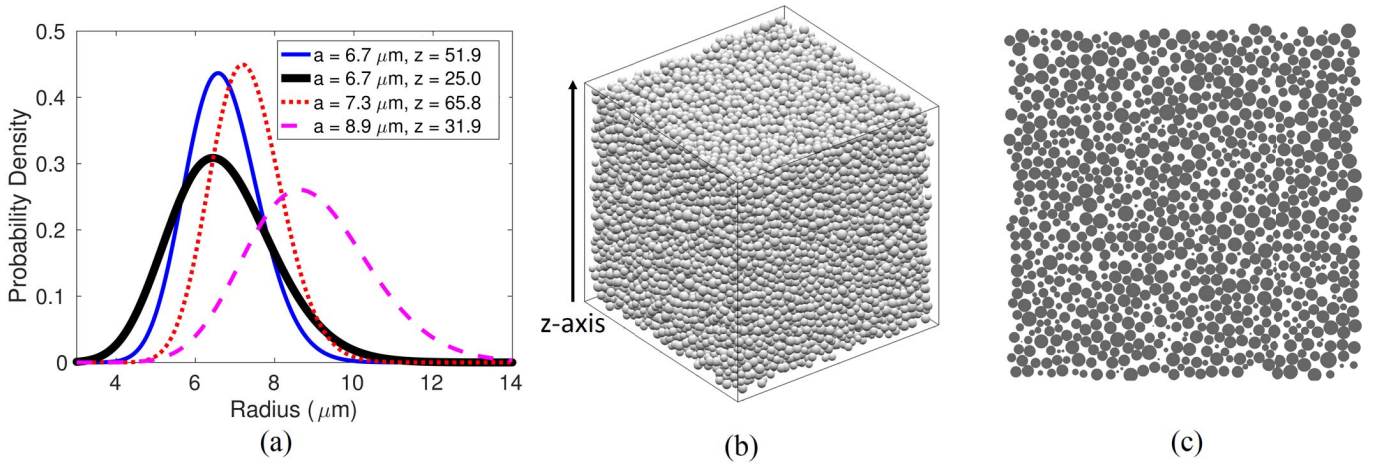


Fig. 1. (a) Probability density functions of the four simulated sphere radius distributions. (b) Simulated 3-D volume of spheres ( $a = 6.7 \mu\text{m}$ ,  $z = 51.9$ ) with a volume fraction 60%. The direction of the  $z$ -axis is indicated by the arrow. (c) 2-D slice of zero thickness generated from the 3-D volume shown in (b).

### B. Simulation Methods

The radii of the simulated spheres followed a  $\Gamma$ -distribution, with a probability density function

$$f_z(x) = \frac{1}{z!} \left( \frac{z+1}{a} \right)^{z+1} x^z e^{-\frac{(z+1)x}{a}} \quad (17)$$

where  $a$  is the mean radius and  $z$  is a parameter inversely related to the distribution width (a larger  $z$  corresponding to a narrower distribution). Four size distributions were simulated [Fig. 1(a)]: 1)  $a = 6.7 \mu\text{m}$ ,  $z = 51.9$ ; 2)  $a = 7.3 \mu\text{m}$ ,  $z = 65.8$ ; 3)  $a = 8.9 \mu\text{m}$ ,  $z = 31.9$ ; and 4)  $a = 6.7 \mu\text{m}$ ,  $z = 25$ .

The spheres were randomly distributed in a cube of a given size  $400 \mu\text{m} \times 400 \mu\text{m} \times 400 \mu\text{m}$  [Fig. 1(b)]. The volume fraction of the spheres was 60%. The random sphere packing algorithm used was a modified forced-biased algorithm that is suitable for the high-volume fraction generation [41]. No sphere overlapping was allowed. The periodic boundary condition was used. Ten slices of the same thickness (0 or  $3 \mu\text{m}$ ) perpendicular to the  $z$ -axis of the simulated cube were picked. Each slice was then a distribution of polydisperse disks [Fig. 1(c)].

The ground truth 3-D SF was calculated from the simulated cube using (5). The 2-D SF was calculated from each of the slices using (5). Then the proposed stereological method was applied to each slice to yield a 3-D SF estimate. A monodisperse distribution was assumed when solving Hanisch's equation.

### C. Simulation Results and Discussion

The disks on the simulated 2-D slice [Fig. 1(c)] appear to have a greater size distribution than those of the spheres in the cube [Fig. 1(b)]. A small fraction of disks have radii close to 0 because of the slicing effect.

The 3-D SF estimated from the slices using the proposed method agreed well with the ground truth calculated directly from the volume for all the four simulated mean sphere radii and sphere radius distributions [Fig. 2(a)–(d)] when the slice thickness was zero, although the agreement for narrower radius distributions [Fig. 2(a) and (b)] was slightly better than

for wider distributions [Fig. 2(c) and (d)]. The agreement was not affected when the slice thickness was changed from 0 to  $3 \mu\text{m}$  [Fig. 2(e), compared with Fig. 2(a)]. Furthermore, the agreement remained when the estimated mean sphere radius used to solve Hanisch's equation was purposely reduced by 10% [Fig. 2(f), compared with Fig. 2(a)], demonstrating that the proposed stereological method is not sensitive to errors in sphere size estimation.

In contrast, the 2-D SF estimated from the slices did not agree as well with the ground truth 3-D SF. The 2-D SF appeared to be shifted toward the lower frequency end compared to the ground truth, which demonstrates the fundamental difference between the 2-D and 3-D cases.

The simulation results also demonstrated that the monodisperse sphere assumption was acceptable when used to solve Hanisch's equation for spheres having a distribution similar to that of cells and nuclei. Using the monodisperse assumption, the 3-D SF derived from 2-D slices performed noticeably better than the 2-D SF in terms of agreement to the ground truth 3-D SF. [Note: Both 3-D SF curves are extremely close compared to the 2-D curve in Fig. 2(a)–(f).]

The 3-D SF computed using the stereological method captures the structure information within a spatial scale limited by the maximum distance ( $r_{\text{max}}$ ) for which the pair correlation function was computed, because the last step of computing the 3-D SF involves integrating (from 0 to  $\infty$ ) a term containing  $g_V(r) - 1$  using (6-c). The estimated 3-D SF is unreliable for frequencies lower than  $c/r_{\text{max}}$  if  $g_V(r) - 1$  does not vanish for  $r > r_{\text{max}}$ . The maximum distance  $r_{\text{max}}$  used herein was  $84 \mu\text{m}$ , which corresponds to a frequency of 18.3 MHz. Therefore, the frequency range starts from 20 MHz in Fig. 2.

## V. CELL PELLET BIOPHANTOM RESULTS AND DISCUSSION

### A. Overview

The cell pellet biophantom [26] is a useful tool to study ultrasonic scattering theories including the SF. Cell pellet biophantoms were constructed by embedding a known number of cells to a bovine plasma and thrombin clot. The concentration of the cell pellet biophantoms can be controlled. Sparse

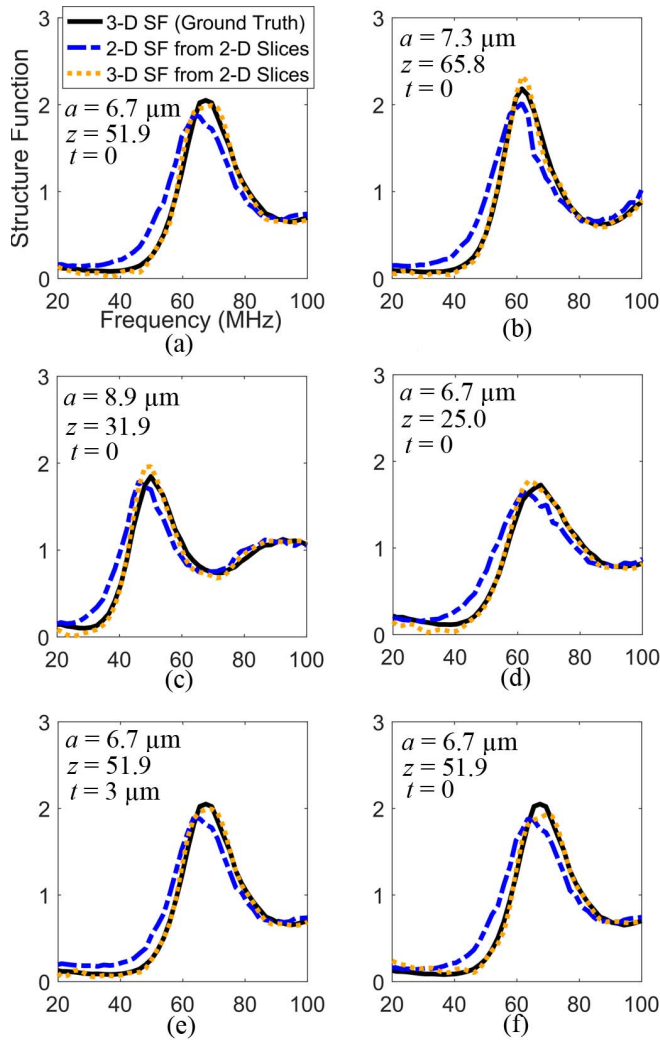


Fig. 2. Comparison between the 2-D SF estimated from 2-D slices (average of 10 slices), 3-D SF estimated using the proposed method (average of 10 slices), and the ground truth 3-D SF from the volume, for four sphere radius distributions. (a), (e), and (f)  $a = 6.7 \mu\text{m}$ ,  $z = 51.9$ . (b)  $a = 7.3 \mu\text{m}$ ,  $z = 65.8$ . (c)  $a = 8.9 \mu\text{m}$ ,  $z = 31.9$ . (d)  $a = 6.7 \mu\text{m}$ ,  $z = 25$ . The slice thickness was  $3 \mu\text{m}$  (e) or 0 (a)–(d) and (f). The estimated mean sphere radius was purposely reduced by 10% when used to compute the 3-D SF from slices in (f) to demonstrate that the method is robust to moderate errors in sphere size estimation. This change was not applied in (a)–(e).

concentrations can be constructed to simulate the case where the cell positions are uncorrelated, and the SF is negligible (SF = 1). Dense concentrations can be constructed to mimic the scattering from solid tumors [39].

Dense cell pellet biophantoms are used to further test the proposed stereological method. The 3-D SF estimated from histology using the proposed method can be compared with the 2-D SF estimated from histology. Furthermore, both the 2-D and 3-D SFs can be compared with the “ground truth” SF derived from QUS measurements. To derive the SF from QUS measurements, a sparse cell pellet biophantom with unity SF is constructed from the same cell line that is used to construct the dense biophantom. “Ground truth” QUS-derived SF is then obtained by taking the ratio of the dense biophantom BSC normalized by number density to the sparse biophantom BSC normalized by number density.

This paper uses existing dense cell pellet biophantom data to test the proposed stereological method. Dense cell pellet biophantoms were constructed in [37], where the QUS-derived SF curves for those biophantoms were published. The histology from that study is used herein to yield the 2-D and 3-D SFs. The details of the cell pellet biophantom experiments were published in [37], and the experimental method is briefly summarized in Section V-B for completeness.

### B. Review of Biophantom Experimental Methods

The biophantoms were composed of a known number of cells clotted in a mixture of bovine plasma and bovine thrombin (Sigma-Aldrich, St. Louis, MO, USA). Three sets of biophantoms were constructed, each made from a different cell line: Chinese hamster ovary [CHO, American Type Culture Collection (ATCC) #CCL-61, Manassas, VA, USA], 13762 MAT B III (MAT, ATCC #CRL-1666), or 4T1 (ATCC #CRL-2539). The mean cell (and nuclear) radii were  $6.7$  ( $3.4$ ),  $7.3$  ( $3.9$ ), and  $8.9$  ( $5.2$ )  $\mu\text{m}$  for CHO, MAT, and 4T1, respectively. Two cell concentrations were constructed for each cell line to be able to derive the SF for the dense biophantom through QUS measurements. Three cell lines were used to validate reproducibility. Each cell line has three realizations to validate repeatability. QUS-derived SFs were obtained over a broad bandwidth (20–100 MHz) using single-element transducers. After ultrasonic data acquisition, the biophantom sample was placed into a histology processing cassette and fixed by immersion in 10% neutral-buffered formalin (pH 7.2) for a minimum of 12 h for histopathologic processing. The sample was then embedded in paraffin, sectioned, mounted on a glass slide, and stained with H&E. An H&E-stained section was viewed under light microscope (Olympus BX-51, Optical Analysis Corporation, Nashua, NH, USA), and a TIF format photograph was taken using the digital camera (Olympus DP25) that was connected with the microscope. The magnification of the objective lens was  $40\times$ . The digitized image had a size of  $1920 \times 1920$  pixels, with a resolution of 5.72 pixels per micrometer. Therefore, the image covered an area of  $336 \times 336 \mu\text{m}^2$  without shrinkage correction.

### C. Application of the Proposed Stereological Method

The four-steps stereological method proposed in Section III were implemented and applied to 45 histological images of CHO, MAT, and 4T1 cell pellet biophantoms, 15 images per cell line. Several implementation details are described and discussed as follows.

A custom MATLAB graphical user interface (GUI) application was developed for semiautomatically fitting circles to cell nuclei on histological images. Fitting circles on an image that contains thousands of cells is challenging. Hough transform circle finding does not work perfectly on histological images—the circle is not always fitted to the cell nuclei. However, it works well when the region of interest (ROI) contains only few cells. Therefore, the challenge of circle fitting is addressed by the developed GUI application that allows the user to draw small rectangular ROIs that collectively cover the entire image.

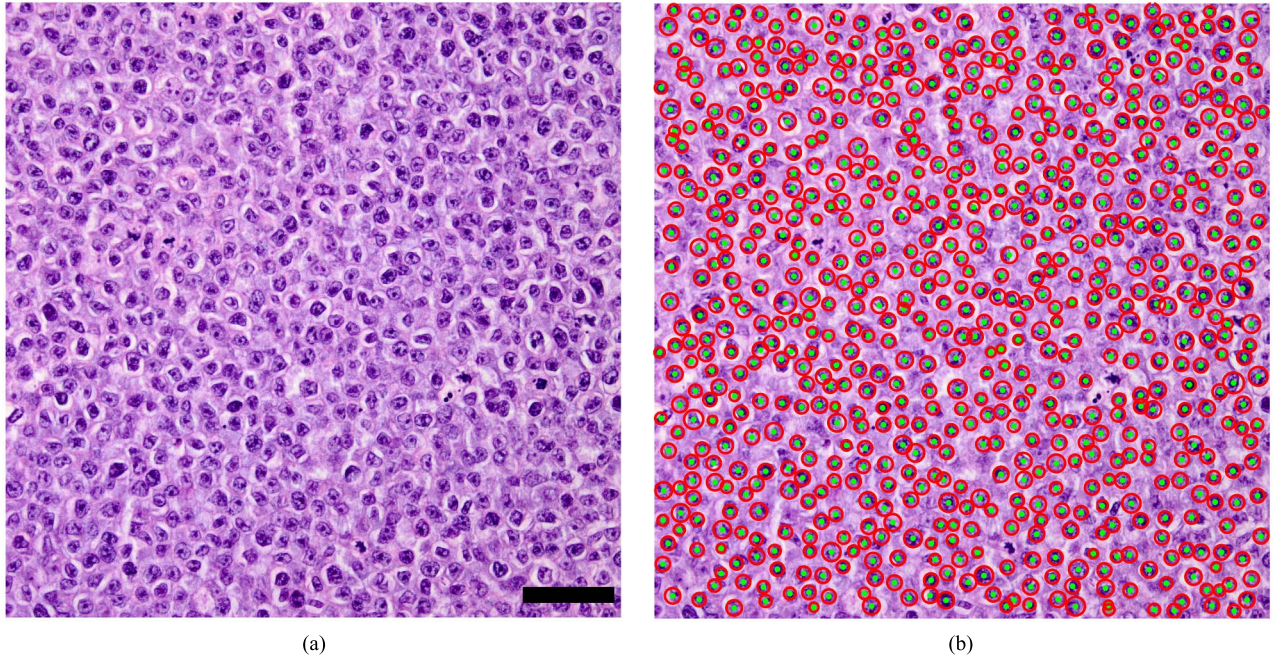


Fig. 3. (a) Digitized H&E-stained histological image (40 $\times$ ) of a high-concentration MAT cell pellet biophantom; the scale bar represents 50  $\mu\text{m}$  without shrinkage correction. (b) Fitted circles (red) and circle centers (green dots) superimposed on the same image.

Circle fitting was performed for each ROI by calling MATLAB function “imfindcircles”. The GUI application allows convenient ROI redrawing and result displaying to make sure that the fitted circles are accurate. Shrinkage correction was performed by assuming a 10% linear shrinkage caused by neutral-buffered formalin fixation [45], [46].

Steps 2–4 of the proposed method were applied as described in Section III. A 3- $\mu\text{m}$  section thickness and constant scatterer diameters were assumed.

To quantitatively evaluate the proposed method, the mean-squared errors (MSEs) were calculated for the histology-derived 3-D SF and the histology-derived 2-D SF, respectively, using the QUS-derived SF as the reference standard. The MSE was defined as

$$\text{MSE} = \sum_{i=1}^M \frac{1}{M} [\text{SF}_s(f_i) - \text{SF}_r(f_i)]^2 \quad (18)$$

where  $\text{SF}_s$  is the SF for which the MSE is to be calculated,  $\text{SF}_r$  is the reference standard,  $f_i$  is the  $i$ th frequency point at which the SFs are evaluated, and  $M$  is the total number of frequency points. The MSEs were calculated for each image.

#### D. Results

An example of the circle fitting results generated using the GUI application is presented in Fig. 3. Visual inspection of Fig. 3 suggests that the GUI application yields accurate circle fitting.

The 3-D SFs estimated using the proposed method are presented in Fig. 4 for CHO, MAT, and 4T1 cell pellet biophantoms, respectively. The corresponding 2-D SFs are also presented for comparison. Each of these histology-derived curves was the average of measurements from 15 images

(three histological sections  $\times$  five images per histological section). Error bars represent 1 standard deviation. The 2-D SFs (Fig. 4) appeared to be shifted toward the lower frequency end compared to the 3-D SFs, an observation that was also made from the simulation results in Fig. 2. The improvement of the 3-D SF over the 2-D one is therefore qualitatively demonstrated through the comparison between Figs. 2 and 4 in terms of the 2-D versus 3-D frequency shift.

The 3-D and 2-D SFs estimated from histology were also compared with the QUS-derived SF in Fig. 4. The 3-D SF appears to be closer to the QUS-derived than does the 2-D SF, which is most noticeable for CHO and MAT and less noticeable for 4T1 (likely due to the high polydispersity of 4T1). The visual observation is also supported by quantitative assessment in terms of MSEs (Fig. 5). The MSEs of the 3-D SFs were statistically significantly lower than those of the 2-D SFs for each cell line based on the Student’s t-test ( $p < 0.001$ ), suggesting that the 3-D SF estimated using the proposed method had statistically significantly better agreement with the QUS-derived SF than did the 2-D SF.

Note that the 2-D SFs in Fig. 4 were not the same as those published in [41, Fig. 3]. The 2-D SF in [41] was calculated from scatterer centers that were manually drawn. Also, shrinkage correction was not applied in [41].

#### E. Discussion

The simulation and biophantom results show that the proposed stereological method for 3-D SF is practical, and yields improved SF estimation than simple 2-D SF estimated from histology. The implementation of the proposed method is straightforward when monodisperse spheres are assumed. Therefore, the proposed stereological method is preferred to the 2-D SF method.

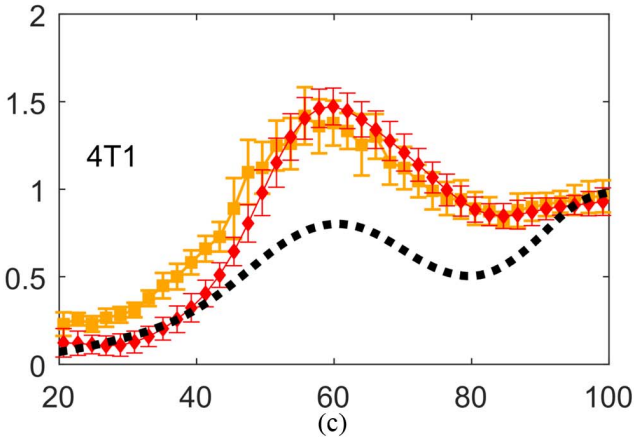
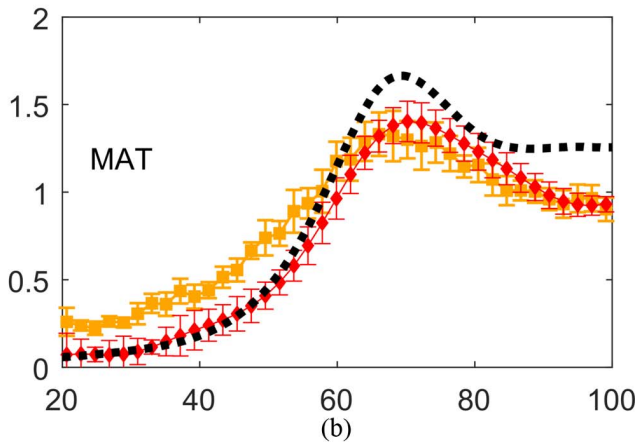
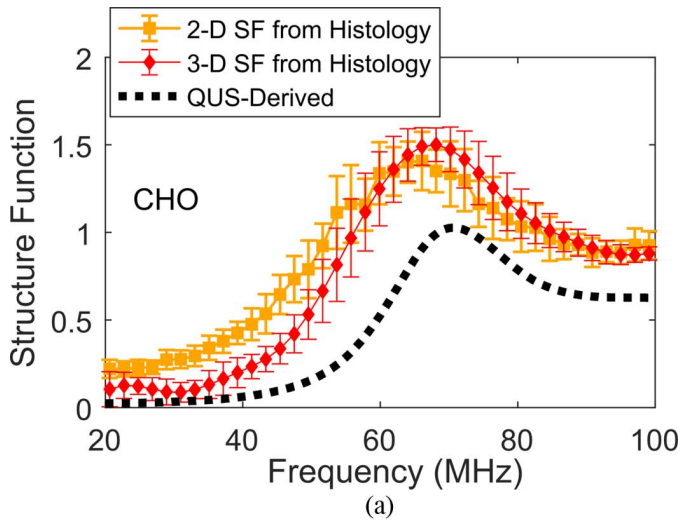


Fig. 4. Comparison between QUS-derived SF (dashed line), the 2-D SF (solid line with squares) estimated from histology, and 3-D SF (solid line with diamonds) estimated using the proposed method from histology for (a) CHO, (b) MAT, and (c) 4T1 cell pellet biophantoms. Each histology-estimated curve represents the average result obtained from 15 histological images obtained from three histological sections (five images per section). Error bars represent one standard deviation. The QUS-derived SFs were previously published [37].

Isotropic distribution and monodisperse spheres are the primary assumptions for the implementation of the proposed method. The isotropic assumption appears to be appropriate for the cell pellet biophantoms (Fig. 3) studied herein. Also,

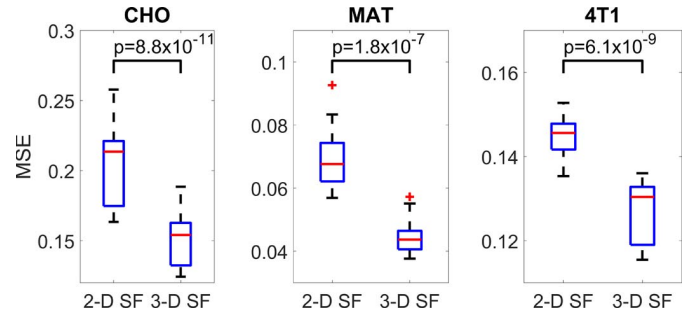


Fig. 5. MSEs of the histology-derived 3-D SFs and 2-D SFs relative to the QUS-derived SF for CHO, MAT, and 4T1 cell pellet biophantoms. The MSEs of the 3-D SFs were statistically significantly lower than those of the 2-D SFs for all the cell lines.

the isotropic assumption holds for the microstructure of a broad range of tissue types such as the liver and solid tumors. However, there are also tissues that exhibit anisotropy, for instance, muscles. The proposed stereological method is not applicable for those tissues. New stereological methods are needed for anisotropic media to take into account the directional dependence of the underlying scatterer distribution.

The monodisperse sphere assumption was tested through simulations. This assumption appears to be reasonable for purposes of implementing the proposed method for the application of biological cells. Alternatively, the proposed method may also be implemented by assuming a distribution (e.g., lognormal distribution) of the sphere size; such an implementation is more sophisticated than the monodisperse implementation, and is not exploited in this paper because the monodisperse assumption was shown by simulation to be close enough.

The thickness of the tissue sections was  $3 \mu\text{m}$ . The section thickness parameter used in the proposed method should be the minimum of the light microscope imaging system's depth of correlation [50] and the tissue section physical thickness. The depth of focus was calculated to be much greater than the tissue section thickness; hence a  $3\text{-}\mu\text{m}$  thickness was appropriate.

The SFs involved in the biophantom study were analyzed based on the nuclei identified by the circle detection algorithm. The SFs based on the whole cells were not evaluated. The cell center and the nuclear center of the same cell are close but not necessarily identical. Therefore, the 3-D SF calculated based on the nuclei should be close to, but not necessarily identical to, that calculated based on whole cells. It will be interesting to evaluate the SFs based on whole cells in the future studies using more advanced automatic cell segmentation algorithms.

The proposed stereological method may be useful in a number of applications. In the QUS context, the method is useful for elucidating the scattering mechanism(s) and identifying the primary scattering sites responsible for scattering. For instance, the SF can be calculated separately for multiple-candidate scattering sites to decide which one agrees with the QUS measures. With widely available H&E-stained tissue sections for various diseases, the proposed method can also be used to predict the SFs of different disease conditions, thereby predicting whether QUS would be sensitive to such

conditions. Also, these histology-derived SFs provide a basis to develop analytical SF models. Last, the proposed method is not limited to acoustic scattering. It is also applicable to other modalities, for example, electromagnetic scattering including light scattering.

Although the proposed method improves the accuracy of SF estimation from histology, the agreement between the resulting 3-D SF and the QUS-derived SF is still not perfect. Future studies may be carried out to investigate such a difference in order to improve the understanding of ultrasonic scattering in tissues. Another direction for the future studies would be to apply the proposed method to various disease conditions to improve the QUS diagnostic ability using the SF.

## VI. CONCLUSION

The proposed stereological method is feasible for estimating the 3-D SF from histology. The proposed method yields a more accurate SF estimate. The 3-D SF estimated using the proposed method has a closer agreement with the QUS-derived SF than does the 2-D SF. The stereological method will be useful for improving the understanding of ultrasonic scattering in tissues and for exploring the diagnostic capability of SF using histology.

## ACKNOWLEDGMENT

The author would like to thank J. R. Kelly for fabricating the cell pellets, and Prof. W. D. O'Brien, Jr., Ph.D., for helpful discussions and critical review of this paper.

## REFERENCES

- [1] E. J. Feleppa, F. L. Lizzi, D. J. Coleman, and M. M. Yaremko, "Diagnostic spectrum analysis in ophthalmology: A physical perspective," *Ultrasound Med. Biol.*, vol. 12, no. 8, pp. 623–631, 1986.
- [2] D. J. Coleman *et al.*, "Noninvasive *in vivo* detection of prognostic indicators for high-risk uveal melanoma: Ultrasound parameter imaging," *Ophthalmology*, vol. 111, no. 3, pp. 558–564, Mar. 2004.
- [3] E. J. Feleppa *et al.*, "Typing of prostate tissue by ultrasonic spectrum analysis," *IEEE Trans. Ultrason., Ferroelect., Freq. Control*, vol. 43, no. 4, pp. 609–619, Jul. 1996.
- [4] M. F. Insana, T. J. Hall, J. G. Wood, and Z.-Y. Yan, "Renal ultrasound using parametric imaging techniques to detect changes in microstructure and function," *Invest. Radiol.*, vol. 28, no. 8, pp. 720–725, 1993.
- [5] J. G. Miller *et al.*, "Myocardial tissue characterization: An approach based on quantitative backscatter and attenuation," in *Proc. Ultrason. Symp.*, Oct./Nov. 1983, pp. 782–793.
- [6] P. K. Tamirisa, M. R. Holland, J. G. Miller, and J. E. Pérez, "Ultrasonic tissue characterization: Review of an approach to assess hypertrophic myocardium," *Echocardiography*, vol. 18, no. 7, pp. 593–597, 2001.
- [7] L. Y. L. Mo and R. S. C. Cobbold, "Theoretical models of ultrasonic scattering in blood," in *Ultrasonic Scattering in Biological Tissues*, K. K. Shung and G. A. Thieme, Eds. Boca Raton, FL, USA: CRC Press, 1993, pp. 125–170.
- [8] F. T. H. Yu, É. Franceschini, B. Chayer, J. K. Armstrong, H. J. Meiselman, and G. Cloutier, "Ultrasonic parametric imaging of erythrocyte aggregation using the structure factor size estimator," *Biorheology*, vol. 46, no. 4, pp. 343–363, 2009.
- [9] M. L. Oelze, W. D. O'Brien, Jr., J. P. Blue, and J. F. Zachary, "Differentiation and characterization of rat mammary fibroadenomas and 4T1 mouse carcinomas using quantitative ultrasound imaging," *IEEE Trans. Med. Imag.*, vol. 23, no. 6, pp. 764–771, Jun. 2004.
- [10] M. L. Oelze and W. D. O'Brien, Jr., "Application of three scattering models to characterization of solid tumors in mice," *Ultrason. Imag.*, vol. 28, no. 2, pp. 83–96, 2006.
- [11] L. A. Wirtzfeld *et al.*, "Techniques and evaluation from a cross-platform imaging comparison of quantitative ultrasound parameters in an *in vivo* rodent fibroadenoma model," *IEEE Trans. Ultrason., Ferroelect., Freq. Control*, vol. 60, no. 7, pp. 1386–1400, Jul. 2013.
- [12] L. A. Wirtzfeld *et al.*, "Quantitative ultrasound comparison of MAT and 4T1 mammary tumors in mice and rats across multiple imaging systems," *J. Ultrasound Med.*, vol. 34, no. 8, pp. 1373–1383, 2015.
- [13] B. S. Garra, M. F. Insana, T. H. Shawker, R. F. Wagner, M. Bradford, and M. Russell, "Quantitative ultrasonic detection and classification of diffuse liver disease. Comparison with human observer performance," *Invest. Radiol.*, vol. 24, no. 3, pp. 196–203, 1989.
- [14] J. Mamou *et al.*, "Three-dimensional high-frequency backscatter and envelope quantification of cancerous human lymph nodes," *Ultrasound Med. Biol.*, vol. 37, no. 3, pp. 345–357, 2011.
- [15] M. C. Kolios, G. J. Czarnota, M. Lee, J. W. Hunt, and M. D. Sherar, "Ultrasonic spectral parameter characterization of apoptosis," *Ultrasound Med. Biol.*, vol. 28, no. 5, pp. 589–597, May 2002.
- [16] H. Banihashemi, R. Vlad, B. Debeljevic, A. Giles, M. C. Kolios, and G. J. Czarnota, "Ultrasound imaging of apoptosis in tumor response: Novel preclinical monitoring of photodynamic therapy effects," *Cancer Res.*, vol. 68, no. 20, pp. 8590–8596, 2008.
- [17] H. Tadayyon, A. Sadeghi-Naini, L. Wirtzfeld, F. C. Wright, and G. Czarnota, "Quantitative ultrasound characterization of locally advanced breast cancer by estimation of its scatterer properties," *Med. Phys.*, vol. 41, no. 1, p. 012903, 2014.
- [18] A. Sadeghi-Naini *et al.*, "Quantitative ultrasound evaluation of tumor cell death response in locally advanced breast cancer patients receiving chemotherapy," *Clin. Cancer Res.*, vol. 19, no. 8, pp. 2163–2174, 2013.
- [19] A. Han, J. W. Erdman, D. G. Simpson, M. P. Andre, and W. D. O'Brien, "Early detection of fatty liver disease in mice via quantitative ultrasound," in *Proc. IEEE Int. Ultrason. Symp.*, Sep. 2014, pp. 2363–2366.
- [20] M. P. Andre *et al.*, "Accurate diagnosis of nonalcoholic fatty liver disease in human participants via quantitative ultrasound," in *Proc. IEEE Int. Ultrason. Symp.*, Sep. 2014, pp. 2375–2377.
- [21] S. C. Lin *et al.*, "Noninvasive diagnosis of nonalcoholic fatty liver disease and quantification of liver fat using a new quantitative ultrasound technique," *Clin. Gastroenterol. Hepatol.*, vol. 13, no. 7, pp. 1337–1345, Jul. 2015.
- [22] B. L. McFarlin *et al.*, "Beyond cervical length: A pilot study of ultrasonic attenuation for early detection of preterm birth risk," *Ultrasound Med. Biol.*, vol. 41, no. 11, pp. 3023–3029, 2015.
- [23] M. F. Insana, R. F. Wagner, D. G. Brown, and T. J. Hall, "Describing small-scale structure in random media using pulse-echo ultrasound," *J. Acoust. Soc. Amer.*, vol. 87, no. 1, pp. 179–192, 1990.
- [24] V. Twersky, "Low-frequency scattering by correlated distributions of randomly oriented particles," *J. Acoust. Soc. Amer.*, vol. 81, no. 5, pp. 1609–1618, 1987.
- [25] I. Fontaine, M. Bertrand, and G. Cloutier, "A system-based approach to modeling the ultrasound signal backscattered by red blood cells," *Biophys. J.*, vol. 77, no. 5, pp. 2387–2399, Nov. 1999.
- [26] M. Teisseire, A. Han, R. Abuhabsah, J. P. Blue, Jr., S. Sarwate, and W. D. O'Brien, Jr., "Ultrasonic backscatter coefficient quantitative estimates from Chinese hamster ovary cell pellet biophantoms," *J. Acoust. Soc. Amer.*, vol. 128, no. 5, pp. 3175–3180, 2010.
- [27] A. Han, R. Abuhabsah, J. P. Blue, Jr., S. Sarwate, and W. D. O'Brien, Jr., "Ultrasonic backscatter coefficient quantitative estimates from high-concentration Chinese hamster ovary cell pellet biophantoms," *J. Acoust. Soc. Amer.*, vol. 130, no. 6, pp. 4139–4147, 2011.
- [28] V. Twersky, "Low-frequency scattering by mixtures of correlated non-spherical particles," *J. Acoust. Soc. Amer.*, vol. 84, no. 1, pp. 409–415, 1988.
- [29] E. Franceschini, R. K. Saha, and G. Cloutier, "Comparison of three scattering models for ultrasound blood characterization," *IEEE Trans. Ultrason., Ferroelect., Freq. Control*, vol. 60, no. 11, pp. 2321–2334, Nov. 2013.
- [30] D. Savéry and G. Cloutier, "A point process approach to assess the frequency dependence of ultrasound backscattering by aggregating red blood cells," *J. Acoust. Soc. Amer.*, vol. 110, no. 6, pp. 3252–3262, 2001.
- [31] D. Savéry and G. Cloutier, "Effect of red cell clustering and anisotropy on ultrasound blood backscatter: A Monte Carlo study," *IEEE Trans. Ultrason., Ferroelect., Freq. Control*, vol. 52, no. 1, pp. 94–103, Jan. 2005.

- [32] R. K. Saha and G. Cloutier, "Monte Carlo study on ultrasound backscattering by three-dimensional distributions of red blood cells," *Phys. Rev. E, Stat. Phys. Plasmas Fluids Relat. Interdiscip. Top.*, vol. 78, no. 6, p. 61919, 2008.
- [33] J. W. Hunt, A. E. Worthington, A. Xuan, M. C. Kolios, G. J. Czarnota, and M. D. Sherar, "A model based upon pseudo regular spacing of cells combined with the randomisation of the nuclei can explain the significant changes in high-frequency ultrasound signals during apoptosis," *Ultrasound Med. Biol.*, vol. 28, no. 2, pp. 217–226, 2002.
- [34] R. M. Vlad, R. K. Saha, N. M. Alajez, S. Ranieri, G. J. Czarnota, and M. C. Kolios, "An increase in cellular size variance contributes to the increase in ultrasound backscatter during cell death," *Ultrasound Med. Biol.*, vol. 36, no. 9, pp. 1546–1558, 2010.
- [35] E. Franceschini and R. Guillermin, "Experimental assessment of four ultrasound scattering models for characterizing concentrated tissue-mimicking phantoms," *J. Acoust. Soc. Amer.*, vol. 132, no. 6, pp. 3735–3747, 2012.
- [36] E. Franceschini, R. Guillermin, F. Tourniaire, S. Roffino, E. Lamy, and J.-F. Landrier, "Structure factor model for understanding the measured backscatter coefficients from concentrated cell pellet biophantoms," *J. Acoust. Soc. Amer.*, vol. 135, no. 6, pp. 3620–3631, 2014.
- [37] A. Han and W. D. O'Brien, Jr., "Structure function for high-concentration biophantoms of polydisperse scatterer sizes," *IEEE Trans. Ultrason., Ferroelect., Freq. Control*, vol. 62, no. 2, pp. 303–318, Feb. 2015.
- [38] E. Franceschini, R. de Monchy, and J. Mamou, "Quantitative characterization of tissue microstructure in concentrated cell pellet biophantoms based on the structure factor model," *IEEE Trans. Ultrason., Ferroelect., Freq. Control*, vol. 63, no. 9, pp. 1321–1334, Sep. 2016.
- [39] A. Han, R. Abuhabsah, R. J. Miller, S. Sarwate, and W. D. O'Brien, Jr., "The measurement of ultrasound backscattering from cell pellet biophantoms and tumors *ex vivo*," *J. Acoust. Soc. Amer.*, vol. 134, no. 1, pp. 686–693, 2013.
- [40] P. Muleki-Seya *et al.*, "High-frequency quantitative ultrasound spectroscopy of excised canine livers and mouse tumors using the structure factor model," *IEEE Trans. Ultrason., Ferroelect., Freq. Control*, vol. 63, no. 9, pp. 1335–1350, Sep. 2016.
- [41] A. Han and W. D. O'Brien, Jr., "Structure function estimated from histological tissue sections," *IEEE Trans. Ultrason., Ferroelect., Freq. Control*, vol. 63, no. 9, pp. 1296–1305, Sep. 2016.
- [42] E. E. Underwood, "The mathematical foundations of quantitative stereology," in *Stereology and Quantitative Metallography*. Philadelphia, PA, USA: ASTM, 1972.
- [43] K.-H. Hanisch, "On stereological estimation of second-order characteristics and of the hard-core distance of systems of sphere centres," *Biometrical J.*, vol. 25, no. 8, pp. 731–743, 1983.
- [44] S. N. Chiu, D. Stoyan, W. S. Kendall, and J. Mecke, *Stochastic Geometry and Its Applications*, 3rd ed. Hoboken, NJ, USA: Wiley, 2013.
- [45] K. F. A. Ross, "Cell shrinkage caused by fixatives and paraffin-wax embedding in ordinary cytological preparations," *J. Microscopical Sci.*, vol. 94, no. 26, pp. 125–139, 1953.
- [46] T. Tran *et al.*, "Correcting the shrinkage effects of formalin fixation and tissue processing for renal tumors: Toward standardization of pathological reporting of tumor size," *J. Cancer*, vol. 6, no. 8, pp. 759–766, 2015.
- [47] J. C. Crocker and D. G. Grier, "Methods of digital video microscopy for colloidal studies," *J. Colloid Interface Sci.*, vol. 179, no. 1, pp. 298–310, Apr. 1996.
- [48] J. Ohser and F. Mücklich, *Statistical Analysis of Microstructures in Materials Science*. Hoboken, NJ, USA: Wiley, 2000.
- [49] L. M. Zurk, L. Tsang, J. Shi, and R. E. Davis, "Electromagnetic scattering calculated from pair distribution functions retrieved from planar snow sections," *IEEE Trans. Geosci. Remote Sens.*, vol. 35, no. 6, pp. 1419–1428, Nov. 1997.
- [50] C. D. Meinhardt, S. T. Wereley, and M. H. B. Gray, "Volume illumination for two-dimensional particle image velocimetry," *Meas. Sci. Technol.*, vol. 11, no. 6, pp. 809–814, 2000.



**Aiguo Han** (S'13–M'15) was born in Jiangsu, China, in 1986. He received the B.S. degree in acoustics from Nanjing University, Nanjing, China, in 2008, and the M.S. and Ph.D. degrees in electrical and computer engineering from the University of Illinois at Urbana–Champaign, Urbana, IL, USA, in 2011 and 2014, respectively.

Since 2015, he has been a Postdoctoral Research Associate with the University of Illinois at Urbana–Champaign. His research interests include ultrasonic wave propagation in heterogeneous media, biomedical ultrasound imaging and quantitative ultrasound, and signal processing and machine learning techniques for ultrasonic tissue characterization.

Dr. Han is a member of the Acoustical Society of America and the American Institute of Ultrasound in Medicine. He was a recipient of the New Investigator Basic Science Award of the 2016 AIUM Annual Convention.